

Large-amplitude Inertia Gravity Waves over Syowa Station: Comparison of PANSY Radar and ERA5 Reanalysis Data

L. Yoshida¹, Y. Tomikawa^{1,2,3}, M. K. Ejiri^{1,2}, M. Tsutsumi^{1,2}, M. Kohma⁴, and K. Sato⁴

¹Polar Science Program, Graduate Institute for Advanced Studies, SOKENDAI, Tachikawa, Japan.

²National Institute of Polar Research, Tachikawa, Japan.

³Polar Environment Data Science Center, Research Organization of Information and Systems, Tachikawa, Japan.

⁴Department of Earth and Planetary Science, The University of Tokyo, Tokyo, Japan.

Corresponding author: Lihito Yoshida (yoshida.rihito@nipr.ac.jp)

Key Points:

- We investigate the large-amplitude gravity wave events over Syowa Station, Antarctica, using PANSY radar and ERA5 reanalysis.
- ERA5 underestimates absolute momentum flux by approximately 1/5 at altitudes of 5–12.5 km; the degree of underestimation increases above 12.5 km.
- Underestimation of absolute momentum flux in ERA5 can be explained by underestimation of the power spectra of horizontal and vertical winds.

Abstract

We examined large-amplitude inertia gravity waves (GWs) over Syowa Station, Antarctica, comparing PANSY radar data and ERA5 reanalysis from October 2015 to September 2016. Focusing on large-amplitude events with a large absolute momentum flux (AMF), hodograph analysis was applied to estimate the wave parameters and found that the percentage of these waves with a downward phase velocity increased with altitude. Vertical wavelengths shortened, intrinsic periods lengthened, and horizontal wavelengths became longer with increasing altitude. Southward propagation of GWs was predominant in the stratosphere. Compared to a previous study, the wave parameters' altitude variation remained consistent, but horizontal and vertical wavelengths were longer in this study. ERA5 underestimated AMF by about 1/5 between 5 and 12.5 km, with a larger underestimation at higher altitudes. The underestimation was related to the power spectra of horizontal and vertical winds, particularly vertical winds. The greater underestimation in the stratosphere might be due to ERA5's vertical grid spacing and shorter vertical wavelengths of dominant GWs.

Plain Language Summary

Gravity waves (GWs) are important waves that influence global wind and temperature structures by transporting momentum but have not been fully reproduced by numerical simulations. This study focuses on GWs over Syowa Station, Antarctica, and compares them between The Program of the Antarctic Syowa MST/IS radar (PANSY) observations and ERA5 reanalysis. The results show that ECMWF Reanalysis v5 (ERA5) underestimates the momentum flux and particularly affected by the vertical wind underestimation. The underestimation of vertical winds may be due to the grid spacing of ERA5, for example.

1 Introduction

Atmospheric gravity waves (GWs) carry momentum to distant regions and drive meridional circulation in the middle atmosphere (stratosphere, mesosphere, and lower thermosphere). The meridional circulation in the mesosphere forms a characteristic temperature structure with low temperatures at the summer pole and high temperatures at the winter pole owing to adiabatic compression and expansion, respectively (Andrews et al., 1987). The (intrinsic) periods of GWs range from the Brunt–Väisälä period (~10 min in the troposphere and ~5 min in the stratosphere), which is the period of buoyant oscillations, to the inertial period, which varies with latitude (~13 h at 69°S where Syowa Station, the focus of this study, is located). The horizontal scales range from a few kilometers to > 1,000 km (e.g., Alexander et al., 2010; Preusse et al., 2008).

GWs can be classified as orographic or nonorographic GWs. Orographic GWs are excited by topography such as mountains (e.g., Eckermann & Preusse, 1999; Kruse et al., 2022; Lott & Miller, 1997; McFarlane, 1987); nonorographic GWs are excited by strong convection (e.g., Ern et al., 2022; Fovell et al., 1992; Pfister et al., 1993; Piani et al., 2000; Song & Chun, 2005; Stephan et al., 2019a,b), jet-front systems (e.g., Charron & Manzini, 2002; Geldenhuys et al., 2021; Kim et al., 2016; Plougonven & Zhang, 2014; Wei et al., 2016; Zhang, 2004; Zülicke & Peters, 2006), and instabilities and auroral heating at high altitudes (Fritts & Alexander, 2003; Oyama & Watkins, 2012). The secondary generation of GWs has also been reported in recent studies (Becker & Vadas, 2018; Kogure et al., 2022; Vadas & Becker, 2023).

An important element that characterizes a GW is its spectrum. The power law for the horizontal and vertical wind spectra is known to universally hold. It is theoretically expected that the slopes of the horizontal and vertical wind frequency spectra are $-5/3$ and $1/3$, respectively (VanZandt, 1982, 1985). Moreover, several factors, including Doppler effects due to background winds and vertical wind shears, can significantly change the frequency spectra (Hocking et al., 2021; Okui et al., 2023; VanZandt et al., 1990). Minamihara et al. (2016) analyzed PANSY radar data at Syowa Station, Antarctica, and found that the spectral slopes of the lower tropospheric horizontal and vertical winds were -1.89 and -1.04 , respectively.

Improved computing power has enabled weather and climate models to achieve higher resolutions and explicitly reproduce some GWs. Nevertheless, it is not possible to reproduce directly the GWs with horizontal and/or vertical scales smaller than the grid spacing of the model. Parameterization is used to compensate for the shortage of the forcing due to unresolved GWs, with assumptions such as steady wave sources and instantaneous vertical propagation of GWs (Alexander & Dunkerton, 1999; Lindzen & Holton, 1968). However, actual wave sources are unsteady and GWs propagate horizontally. Thus, the current parameterization does not represent the meridional propagation, transience, or secondary generation of GWs. For example, the convergence of GW momentum flux into the polar night jet (Sato et al., 2009) is not well represented in most current climate models because of the absence of meridional propagation in the GW parameterization. This leads to weaker GW drag in the model than in the real atmosphere and causes a cold bias in the winter lower stratosphere and a delay in polar vortex breakup (McLandress et al., 2012).

The representation of GWs in models and objective analyses (i.e., operational analysis and reanalysis) has been examined by comparison with observations from balloons, radar, and satellites (e.g., Ern et al., 2022; Jewtoukoff et al., 2015). These studies mostly focused on the statistical features of GWs, such as the horizontal and vertical distributions of GW kinetic and potential energy and (absolute) momentum flux. Jewtoukoff et al. (2015) compared data from super-pressure balloon observations made over Antarctica with those of operational analysis with a horizontal resolution of ~ 80 km and showed that the mean momentum flux of the operational analysis underestimated that of the balloon observations by approximately a factor of five. In addition, the occurrence rate of GW events with large momentum fluxes was lower in the operational analysis.

The Program of the Antarctic Syowa MST/IS radar (PANSY) is the only large-aperture MST/IS radar over Antarctica that can capture GWs over the entire frequency range in the troposphere and lower stratosphere (Sato et al., 2014). Minamihara et al. (2018) examined the characteristics of inertia GWs over Syowa Station using the PANSY radar and showed that inertia GWs observed over Syowa Station are generated by several types of sources, including topography, tropospheric jets, and polar-night jets. In addition, Minamihara et al. (2020) examined the intermittency of GWs over Syowa Station using PANSY radar and indicated that the probability distribution of the GW momentum flux over Syowa Station was different from past super-pressure balloon observations (Hertzog et al., 2012). They inferred that this was because the primary wave source of orographic GWs at Syowa Station is a steady katabatic wind from the northeast direction, whereas on the Antarctic Peninsula, the main source is strong winds caused by synoptic-scale disturbances.

In this study, we examined the characteristics of GWs, especially large-amplitude inertia GWs, over Syowa Station using PANSY radar data and ERA5 reanalysis data. In particular, we

focused on the absolute momentum flux (AMF) and discussed difference in AMF between PANSY and ERA5. The remainder of this paper is organized as follows. Descriptions of the PANSY radar and ERA5 data used in this study are provided in Section 2. The methods used for the hodograph analysis and extraction of GW events are described in Section 3. The results of the statistical analysis are presented in Section 4 and discussed in Section 5. Finally, a summary and concluding remarks are presented in Section 6.

2 Data

2.1 PANSY radar observations

The PANSY radar is a mesosphere–stratosphere–troposphere (MST) radar installed at Syowa Station (69.0°S, 39.6°E) in 2011. It can observe three-dimensional wind vectors in the troposphere and lower stratosphere with high temporal and vertical resolutions (Sato et al., 2014).

Five beams are used in PANSY radar observations, which are pointing to the vertical and to the north, east, south, and west at the same zenith angle of 10°. Vertical wind velocities are estimated directly from the vertical beam, and the east–west (north–south) component is obtained from the line-of-sight velocity of the east–west (north–south) beam. The accuracy of wind velocity is approximately 0.1 ms⁻¹ for vertical wind and approximately 0.5 ms⁻¹ for east–west and north–south wind. The spatial resolution along the beam direction is approximately 150 m. Beam width is approximately 1.0°, corresponding to a horizontal width of approximately 350 m at an altitude of 20 km. The time resolution of tropospheric and stratospheric observations is approximately 200 s. In this study, we used 3-dimensional wind velocities estimated from echo spectra incoherently integrated over 30 min since the 30-min integrated data can extend the upper limit of the observation altitude range by 3–5 km. For comparison with ERA5, the 30-min integrated data were interpolated to hourly intervals.

The data used in this study correspond to the period of continuous observations performed from October 1, 2015, to September 30, 2016. Such long-term continuous observations are unprecedented at other latitudes and reveal seasonal changes in the intermittency and vertical distribution of GWs over Syowa Station (Minamihara et al., 2018, 2020).

2.2 ERA5 reanalysis

ERA5 is the latest atmospheric reanalysis dataset provided by the European Centre for Medium-Range Weather Forecasts (ECMWF) (Hersbach et al., 2020). The data are provided on 137 model levels vertically from the surface up to the pressure level of 0.01 hPa (~80 km altitude). The altitude interval in the troposphere and lower stratosphere (~1.5 to 20 km), which was the focus of this study, ranges from 150 to 400 m. The latitude and longitude intervals were 0.25° × 0.25°, and the time interval was 1 h. Data from the grid point closest to Syowa Station (69.0°S, 39.5°E) were used for analysis. We confirmed that the analysis results using the data of the other three grid points surrounding Syowa Station (69.0°S, 39.75°E; 69.25°S, 39.5°E; and 69.25°S, 39.75°E) did not significantly change.

Figure 1 shows the time–altitude cross sections of zonal and vertical winds from PANSY and ERA5 for January 2016. The ERA5 zonal wind is in good agreement with the PANSY zonal wind both in magnitude and phase structure (Fig. 1a and 1b). While the vertical wind in ERA5

shows large-amplitude disturbances at nearly the same time as that in PANSY (e.g., ~1.5 to 10 km around January 9, 13, 20, and 30), the amplitudes of the disturbances in ERA5 are much smaller than those in PANSY (Fig. 1c and 1d).

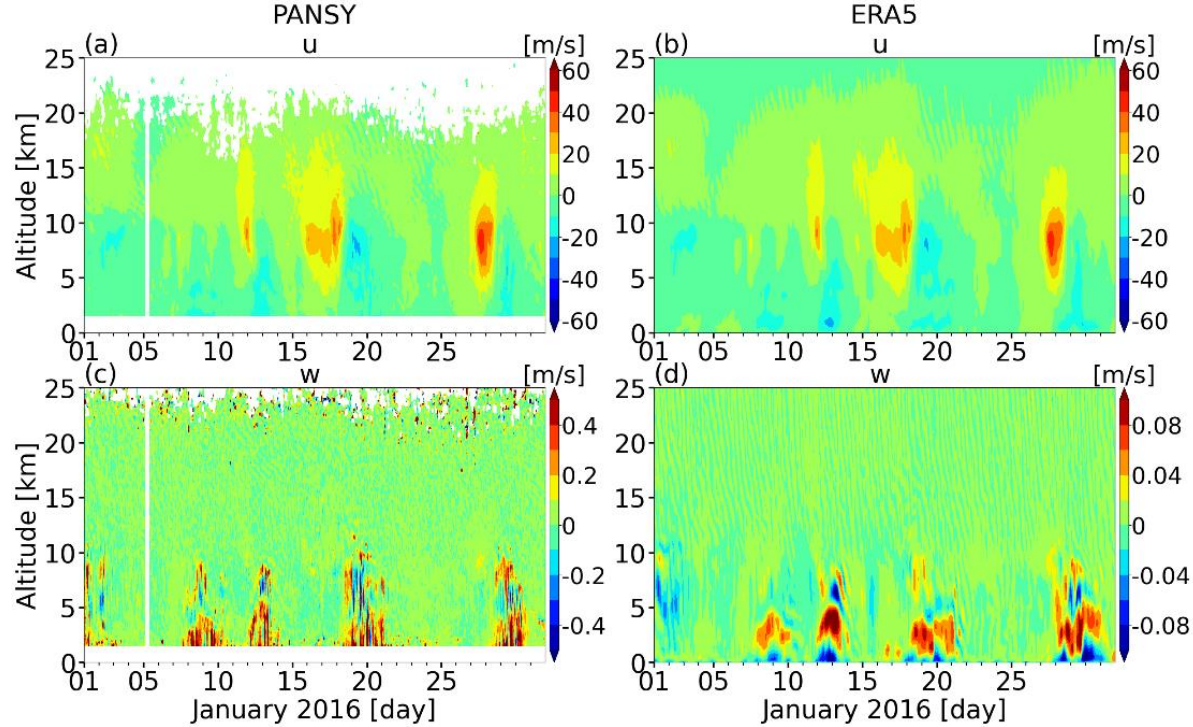


Figure 1. Time–altitude cross sections of zonal (a, b) and vertical (c, d) winds from PANSY (a, c) and ERA5 (b, d) for January 2016.

3 Method

3.1 Extraction of GWs

The intrinsic period of GWs ranges from the Brunt–Väisälä period (i.e., ~5 min in the stratosphere and ~10 min in the troposphere) to the inertial period (i.e., ~13 h at Syowa Station). Since hourly 3-dimensional wind data were analyzed, we focused on inertia GWs. To extract inertia GWs, a bandpass filter with cutoff periods of 4 and 24 h was applied to the data, as in Minamihara et al. (2020). In addition, since the vertical wavelengths of inertia GWs over Syowa Station are mostly 1–5 km (Minamihara et al., 2018), a bandpass filter with cutoff vertical wavelengths of 0.8 and 8 km was also applied. Time–altitude cross-sections of filtered wind data often show superposition of wave-like structures with upward and downward phase propagation (e.g., Fig. 6 of Minamihara et al., 2018). This feature makes it difficult to estimate GW parameters using hodograph analysis, because it assumes that the wind disturbance is due to a monochromatic GW. To obtain wave components as monochromatically as possible, a two-dimensional (i.e., temporal and vertical) Fourier series expansion was applied to the wind data. Then, wind disturbances with upward phase velocities ($C_z > 0$) and downward phase velocities ($C_z < 0$) were obtained separately (Yoshiki et al., 2004).

Figure 2 shows the time–altitude cross sections of zonal and vertical wind disturbances with $C_z < 0$ from PANSY and ERA5 in January 2016. Comparing the zonal wind disturbances between PANSY and ERA5, the phase and amplitude of wave-like events were generally

consistent in the troposphere. However, some events, such as those between January 17 and 22 around an altitude of 18 km, showed a similar phase structure, but their amplitudes were significantly different (Fig. 2a and 2b). A comparison of the vertical wind disturbances shows that ERA5 failed to reproduce the wave-like events observed in the PANSY observations between January 17 and 22 at an altitude of 18 km (Fig. 2c and 2d). The meridional wind disturbances with $C_z > 0$ components showed features similar to the zonal wind disturbances with $C_z < 0$ components (not shown).

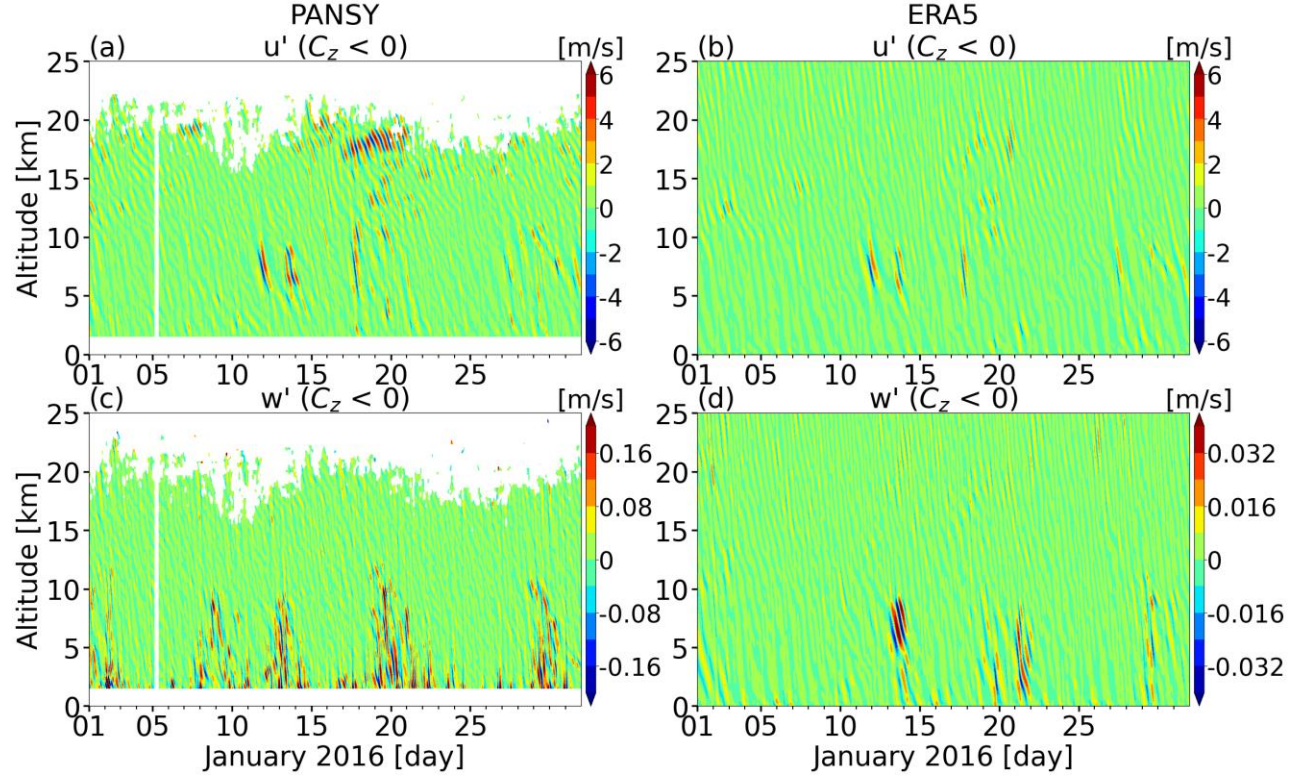


Figure 2. Same as Fig. 1 except for wind disturbances with downward phase velocities ($C_z < 0$).

Hodographs depict the altitude variation of horizontal wind disturbance vectors in velocity space. They are elliptical for inertia GW (Hirota and Niki, 1985). The direction of the major axis indicates the direction of the horizontal wavenumber vector with an ambiguity of 180° . The direction of rotation of the hodograph with altitude indicates the direction of the vertical propagation of energy (i.e., vertical group velocity). When the rotation is counterclockwise (clockwise) with the altitude in the Southern Hemisphere, the energy propagation is upward (downward). The radii of the major and minor axes of the ellipse represent the amplitudes of horizontal wind disturbances parallel and perpendicular to the horizontal wavenumber vector (\tilde{u} , \tilde{v}), respectively. The altitude width of one rotation of the hodograph represents the vertical wavelength. The polarization relation for inertia GWs gives the intrinsic angular frequency $\hat{\omega}$ s^{-1} as follows:

$$|\hat{\omega}| = \left| \frac{\tilde{u}}{\tilde{v}} f_i \right|. \#(1)$$

The dispersion relation for inertia GWs under the hydrostatic approximation is

$$\hat{\omega}^2 = f_i^2 + \frac{N^2 K^2}{m^2}, \#(2)$$

where f_i is the inertial frequency (i.e., $1.36 \times 10^{-4} \text{ s}^{-1}$ corresponding to the inertial period of 12.8 h at Syowa Station), N is the Brunt–Väisälä frequency, m is the vertical wavenumber, and K is the horizontal wavenumber. Note that K can be estimated using equation (2). The ground-based angular frequency ω is obtained from the equation of Doppler shift given by $\omega = \hat{\omega} + UK$. The direction of the horizontal wavenumber vector (θ) is uniquely determined by:

$$\text{sgn}(K) = -\text{sgn}(u_{\parallel}' w') \cdot \text{sgn}(m) \#(3)$$

where u_{\parallel}' is the horizontal wind disturbance parallel to the horizontal wavenumber vector, w' is the vertical wind disturbance and $u_{\parallel}' w'$ is the covariance.

Although a hodograph can be drawn from a vertical profile at one time, in our analysis, a single hodograph was drawn using vertical profiles at multiple times to improve the fitting accuracy. Figure 3 shows example hodographs for PANSY and ERA5. The x-axis and y-axis show the zonal and meridional wind components, respectively. Each filled circle represents a data point, color represents time in UT on September 22, 2016, and the black line represents a fitted ellipse.

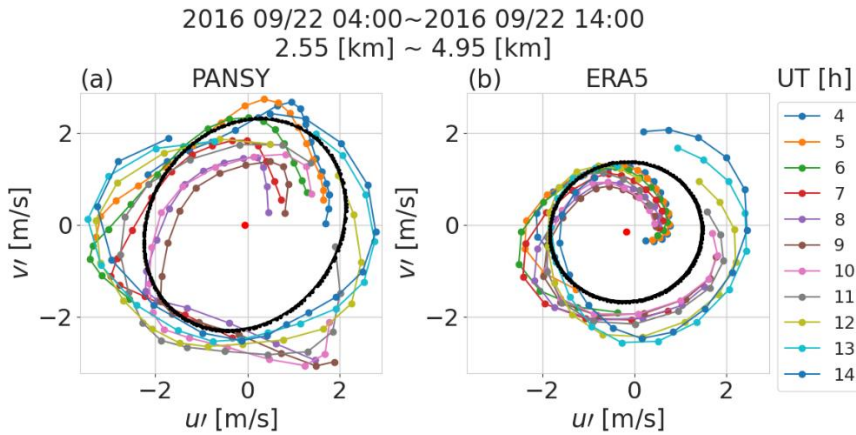


Figure 3. Results of the hodograph analysis applied to (a) PANSY and (b) ERA5 data in the height range of 2.55–4.95 km at 0400–1400 UT on 22 September 2016 (dots – data, black line – fitted ellipse, red point – center of fitted ellipse).

3.3 AMF estimation

Absolute momentum flux (AMF) was used to compare the PANSY radar and ERA5 data. AMF was estimated using three types of methods.

(1) AMF was estimated from GW parameters obtained by the hodograph analysis as follows:

$$\text{AMF} = \left| \frac{\bar{\rho} \tilde{u} \tilde{w}}{2} \right| \#(4)$$

Where, $\tilde{w} = -\frac{K}{m} \frac{\bar{\omega}^2 - f_l^2}{N^2 - \bar{\omega}^2}$.

This method was applied to both of PANSY radar and ERA5 data.

(2) AMF was estimated directly from the horizontal and vertical wind disturbances of ERA5, as follows:

$$\text{AMF} = \bar{\rho} \sqrt{(\overline{u'w'})^2 + (\overline{v'w'})^2} \#(5)$$

This method was not applied to the PANSY radar data, because the different beams used to measure the horizontal and vertical winds captured different air masses.

(3) AMF was estimated from line-of-sight velocity along the radar beam direction (Vincent and Reid, 1983), as follows:

$$\text{AMF} = \bar{\rho} \sqrt{\left(\frac{\overline{u_1'^2} - \overline{u_2'^2}}{2 \sin 2\theta} \right)^2 + \left(\frac{\overline{v_1'^2} - \overline{v_2'^2}}{2 \sin 2\theta} \right)^2} \#(6)$$

where u'_1, u'_2, v'_1 , and v'_2 are line-of-sight velocity perturbations towards the east, west, north, and south, respectively, and θ is the angle of the oblique beam from zenith, which is 10° for the PANSY radar. This method enabled us to estimate AMF with greater accuracy than the aforementioned methods.

Figure 4 shows time–altitude cross section of AMF with $C_z < 0$ in January 2016 calculated by the (Fig. 4a) third and (Fig. 4b) second methods. Large AMF events observed by the PANSY radar were roughly captured using the ERA5 data. However, in most cases, the magnitudes were several times larger for PANSY than they were for ERA5.

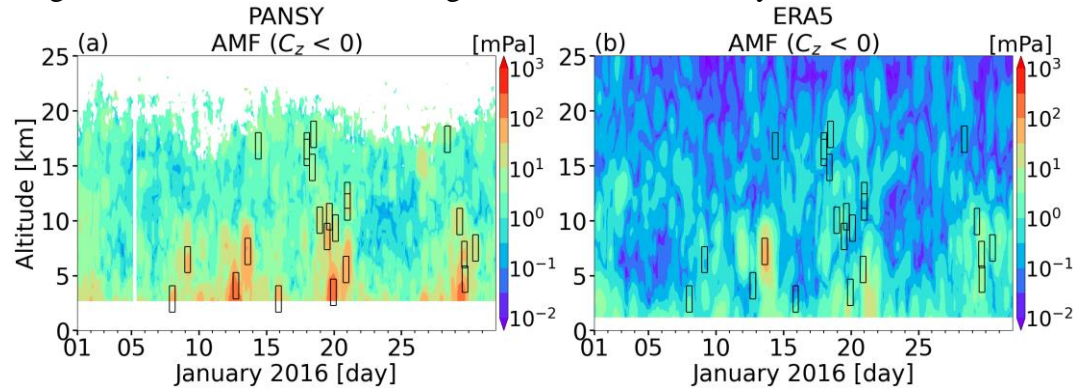


Figure 4. Time–altitude cross section of AMF with $C_z < 0$ in January 2016. AMF was calculated using Eq. 6 from PANSY (a) and Eq. 5 from ERA5 (b). Black rectangles show the identified large-amplitude events with PANSY data.

3.4 Event identification criteria

In this study, we focused on large-amplitude inertia GW events identified from PANSY and ERA5 data using the following procedures:

1. The calculation of the AMF using data with a time interval of 10 h and an altitude range of 2.5 km was repeated by shifting the time and altitude by one step (i.e., 1 h and 150 m, respectively) for both of $C_z > 0$ and $C_z < 0$.
2. Hodograph analysis was applied only to the top 10% of cases with a large AMF (calculated using Eq. 6) at each altitude.
3. When the explained variance was greater than twice the mean square of the residuals, the case was considered quasi-monochromatic.
4. When the aspect ratio of the hodograph was > 0.1 and < 0.9 , and the horizontal wind amplitude perpendicular to the horizontal wavenumber vector (i.e., short radius of the hodograph) was $> 0.5 \text{ ms}^{-1}$, hodograph analysis successfully estimates the parameters of inertia GWs (e.g., Minamihara et al., 2018).
5. Cases adjacent to each other in the time and altitude directions were considered one GW event.

Consequently, 231 and 362 GW events with $C_z > 0$ and $C_z < 0$, respectively, were identified using PANSY radar data. Of these, 59 and 191 events with $C_z > 0$ and $C_z < 0$, respectively, were identified from the ERA5 data.

Figure 5 shows the seasonal variation in the number of GW events identified in the troposphere (below 8 km altitude), tropopause (8–12 km altitude), and stratosphere (above 12 km altitude) from the PANSY radar data. Separation of the height region was determined based on a previous study of tropopause height above Syowa Station (Tomikawa et al., 2009). The upward- and downward-propagating components (i.e., $C_z > 0$ and $C_z < 0$) were also separated. In the troposphere, the number of identified GW events was similar for $C_z > 0$ and $C_z < 0$ and the significant seasonal variation is not observed. In the stratosphere, the number of $C_z < 0$ events are maximized in the austral fall (i.e., MAM) and is greater than $C_z > 0$ events throughout the year. The number of $C_z > 0$ events in the stratosphere is maximized in the austral winter (i.e., JJA) and minimized in the austral summer (i.e., DJF). The tropopause region has a larger number of GW events for $C_z < 0$ and small seasonal variation, of which features are intermediate

between the troposphere and stratosphere.

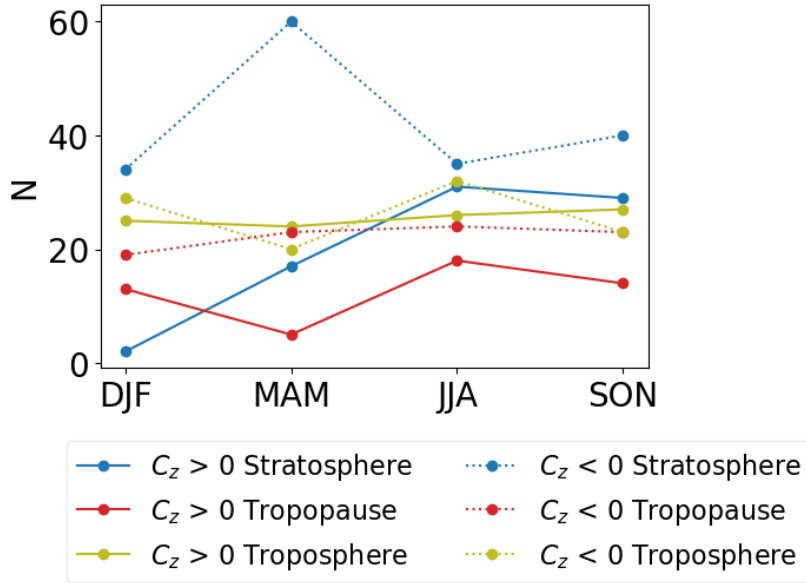


Figure 5. Seasonal variation in the number of identified GW events in the troposphere (olive; below 8 km), tropopause (red; 8~12 km), and stratosphere (blue; above 12 km) from the PANSY radar data. Solid and dashed lines denote $C_z > 0$ and $C_z < 0$ events, respectively.

The division based on the vertical phase velocity in this analysis does not necessarily coincide with that based on the vertical group velocity. The vertical phase and group velocities (C_z and C_{gz} , respectively) are given by:

$$C_z = \frac{\omega}{m} = \frac{\hat{\omega} + KU}{m}, \#(7)$$

$$C_{gz} = -\frac{m(\hat{\omega}^2 - f_t^2)}{\hat{\omega}(K^2 + m^2)}. \#(8)$$

where U denotes the background wind parallel to the horizontal wave number vector. These equations indicate that if the background wind is weak, the vertical phase and group velocities will be in opposite directions; however, if the background wind is sufficiently strong in the opposite direction of the horizontal wavenumber vector, the vertical phase and group velocities will be in the same direction. In our analysis, almost all GW events with $C_z < 0$ had $C_{gz} > 0$, whereas approximately half of the GW events with $C_z > 0$ had $C_{gz} > 0$.

4 Results

4.1 AMF

Figure 6 shows the vertical profiles of the AMF ratio between PANSY and ERA5 ($\text{AMF}_{\text{ERA5}}/\text{AMF}_{\text{PANSY}}$ as AMF ratio (ERA5/PANSY)). $\text{AMF}_{\text{PANSY}}$ and AMF_{ERA5} were calculated using Eq. 6 and Eq. 5, respectively, for $C_z > 0$, $C_z < 0$, and their sum. The ratio is larger around 5–12.5 km and decreases with altitude above 12.5 km for $C_z > 0$, $C_z < 0$, and their sum. The

ratio of the sum of $C_z > 0$ and $C_z < 0$ is approximately 0.2 from 5 to 12.5 km, but reaches ~ 0.05 at around 20 km. The ratio of $C_z < 0$ is greater than that of $C_z > 0$ at all heights. These features are common across all seasons (data not shown). Whereas the magnitude of AMF for both PANSY and ERA5 increased with altitude up to 15 km, it decreased with altitude above 15 km only for ERA5 (data not shown).

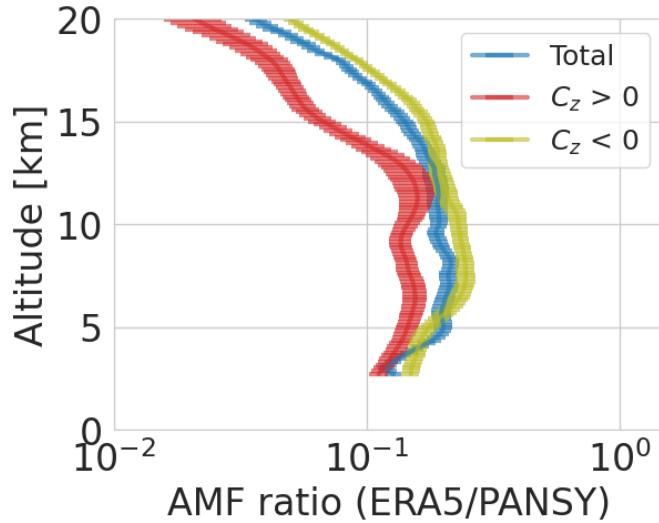


Figure 6. Vertical profiles of the AMF ratio (ERA5/PANSY) for $C_z > 0$ (red), $C_z < 0$ (olive), and their total (blue). Error bars indicate the standard deviation obtained by calculating the AMF for each grid and taking into account the degrees of freedom.

4.2 Spectra

Figure 7 shows the frequency spectra of the zonal and vertical winds from PANSY and ERA5 in the troposphere (Fig. 7a) and stratosphere (Fig. 7b). From left to right, total, $C_z > 0$, and $C_z < 0$ components are plotted. Their spectral slopes were calculated using the spectra from $\omega = 2\pi/4$ h to $\omega = f_i$ by linear least square fitting (shown by gray dashed lines). The exponents are also presented herein. As these spectra were drawn in an energy-content form (i.e., frequency times power spectrum), their exponents were those obtained from the power spectrum plus one. The meridional winds show features similar to those of the zonal winds (not shown).

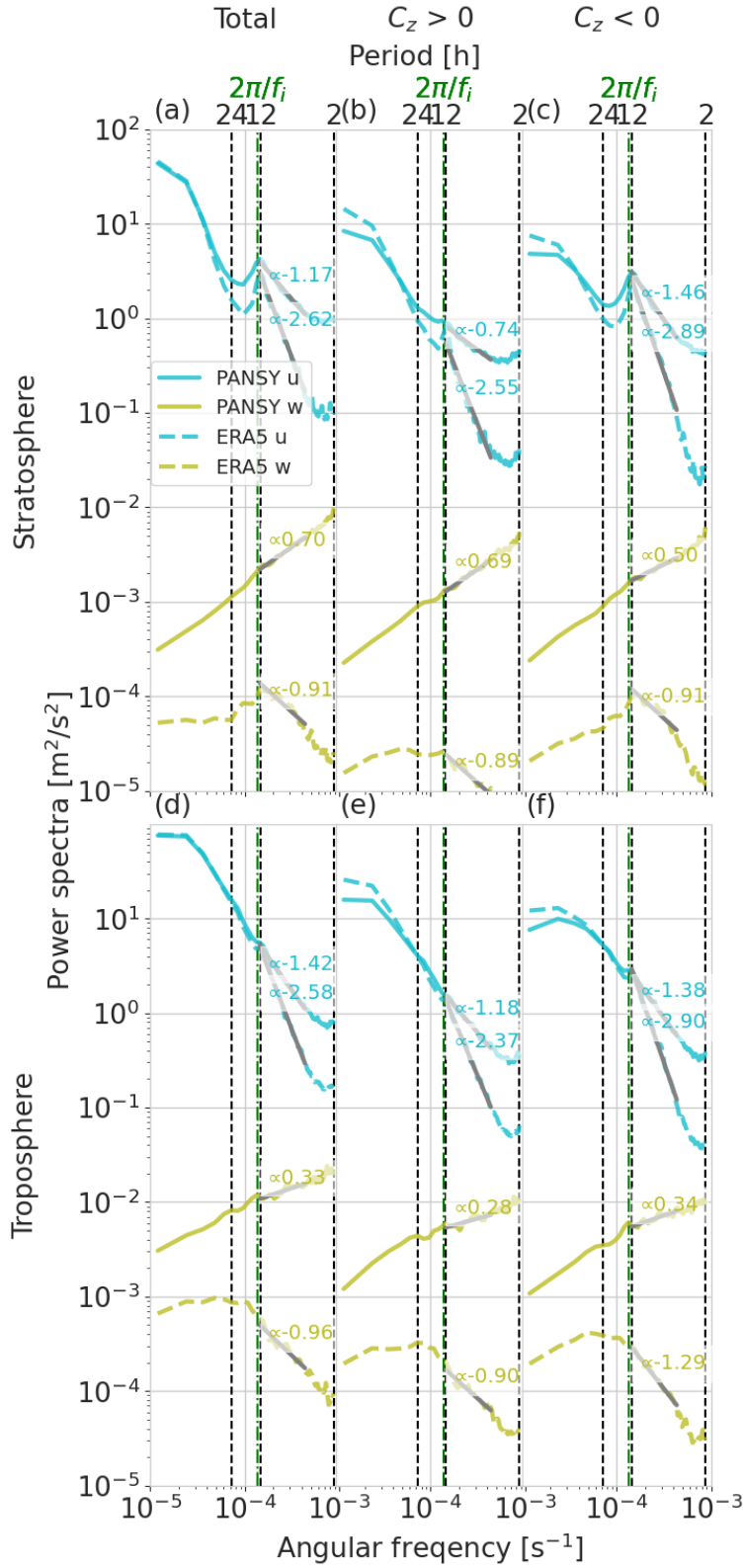


Figure 7. Frequency spectra (energy-content form) of zonal and vertical winds from PANSY and ERA5 in the troposphere (d, e, f) and stratosphere (a, b, c). From left to right, total (a, d), $C_z >$

0(b, e), and $C_z < 0$ (c, f) components are plotted. Their spectral slopes were calculated using the spectra from $\omega = 2\pi/4$ h to $\omega = f_i$ by linear least square fitting (gray dashed lines). Their exponents are also shown.

Power spectra of zonal winds show a good agreement between PANSY and ERA5 for the period longer than the inertial period (i.e., $\omega < f_i$) both in the troposphere and stratosphere for all “total,” $C_z > 0$, and $C_z < 0$. On the other hand, the spectral slope is steeper for ERA5 in the period shorter than the inertial period (i.e., $\omega > f_i$), which suggests that the amplitude of GWs in ERA5 is underestimated for the shorter wave periods. Another interesting feature is that a clear spectral peak is seen near the inertial period only in the stratosphere for “total” and $C_z < 0$. ERA5 shows a weak spectral peak near the inertial period even for $C_z > 0$, unlike PANSY.

The power spectra of vertical winds show features that are clearly different from those of zonal wind. The spectral power of PANSY is one order of magnitude greater than that of ERA5 at all frequencies. In addition, the spectra from PANSY has a positive slope at all frequencies, while those from ERA5 shows a negative slope on the high frequency side (i.e., $\omega > f_i$). These features are common both in the troposphere and stratosphere for all “total,” $C_z > 0$, and $C_z < 0$.

4.3 Hodograph analysis

The statistical properties of the identified GW events were investigated based on the hodograph analysis results. In total, 593 GW events were identified from the PANSY radar data, but only 250 GW events satisfied the identification conditions of GW events for both PANSY and ERA5 (see section 3.4).

First, the AMF obtained from each of the methods (see section 3.3) were compared (Table 1 and Table 2). P1 and E1 represent AMF obtained using Eq. 4 for PANSY and ERA5, respectively. P2 and E2 represent AMF obtained using Eq. 6 for PANSY and Eq. 5 for ERA5, respectively. As P1 and E1 estimates were based only on horizontal winds, their comparison reveals the consistency between the horizontal winds of identified GW events for PANSY and ERA5. The comparison of P2 and E2 reveals the consistency of both horizontal and vertical winds between PANSY and ERA5. If E1 (E2) was more than half of P1 (P2) and less than twice as large as P1 (P2), the two were considered sufficiently close [i.e., $P1(P2) \approx E1(E2)$].

As shown in Table 1, $P1 > E1$, $P1 \approx E1$, and $P1 < E1$ are 50–65%, 20–25%, and 5–25%, respectively for both $C_z > 0$, and $C_z < 0$. This indicates that ERA5 tends to slightly underestimate the horizontal wind amplitudes of identified GW events compared with PANSY. However, as shown in Table 2, E2 is almost always significantly smaller than P2 for both $C_z > 0$, and $C_z < 0$. This suggests that ERA5 tends to significantly underestimate the vertical wind amplitudes of identified GW events.

Table 1. Number of events of $P1 > E1$, $P1 \approx E1$, and $P1 < E1$ for $C_z > 0$ and $C_z < 0$.

	P1 \approx E1	P1 > E1	P1 < E1	Total
$C_z > 0$	13	33	13	59
$C_z < 0$	47	127	17	191

Total	60	160	30	250
-------	----	-----	----	-----

Table 2. Same as Table 1 but comparison of P2 and E2 amplitudes.

	P2 \approx E2	P2 > E2	P2 < E2	Total
$C_z > 0$	8	51	0	59
$C_z < 0$	10	181	0	191
Total	18	232	0	250

Figure 8 shows the scatter plots of aspect ratio (i.e., $|f_i/\hat{\omega}|$), and vertical wavelengths (λ_z) and horizontal wavelengths (λ_h) obtained from hodograph analysis as a function of altitude. The aspect ratio approaches unity with increasing altitude, which suggests that the intrinsic wave period approaches the inertial period. This tendency is common to PANSY and ERA5 but appears only for $C_z < 0$ (not shown). The vertical wavelength decreases with increasing altitude for both PANSY and ERA5. However, the vertical wavelength of ERA5 is 100~400 m longer than that of PANSY at every altitude.

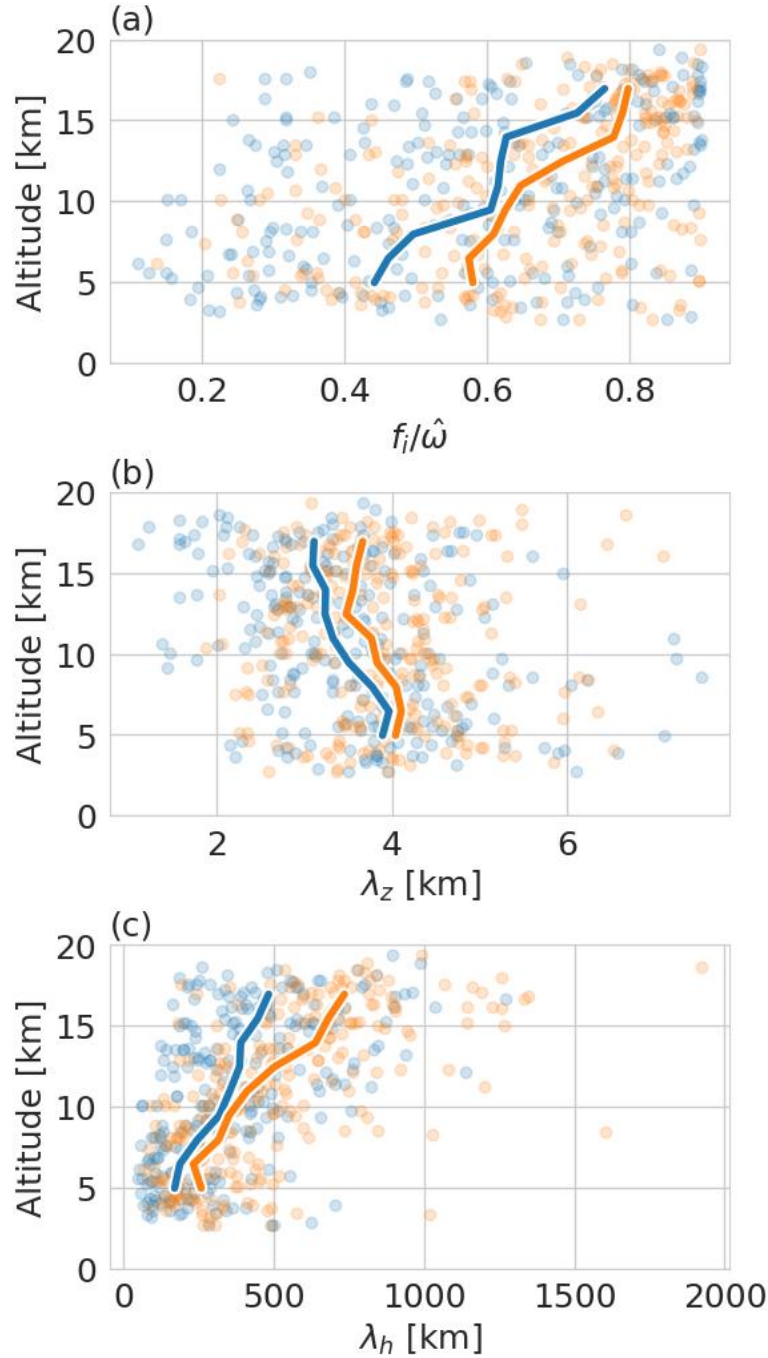


Figure 8. Scatter plots of (a) aspect ratio (i.e., $|f_i/\hat{\omega}|$), (b) vertical wavelengths (λ_z) and (c) horizontal wavelengths (λ_h) obtained from hodograph analysis as a function of altitude. Blue and orange dots denote PANSY and ERA5 data, respectively; solid lines show their median values that are taken every 1.5 km.

Horizontal wavelength increases with increasing altitude for both PANSY and ERA5. In addition, it is longer for ERA5 than for PANSY at all altitudes. The difference is due to the

longer intrinsic wave period and longer vertical wavelength in ERA5 because the horizontal wavelength is obtained from the dispersion relation by the following equation:

$$\begin{aligned}\lambda_h &= 2\pi \sqrt{(\hat{\omega}^2 - f_i^2) * \frac{m^2}{N^2}}^{-1} \\ &= 2\pi \sqrt{\left(\left(f_i * \frac{r_a}{r_b}\right)^2 - f_i^2\right) * \frac{m^2}{N^2}}^{-1} \\ &= \lambda_z \left\{ \left(\frac{r_b}{r_a}\right)^{-2} - 1 \right\}^{-1/2} . \#(9)\end{aligned}$$

Figure 9 shows radar charts of propagation directions (east, west, north, and south) of GWs from Total (i.e., all altitudes), each altitude of PANSY, and each altitude of ERA5. Southward propagation is the most frequent in all altitude regions for both PANSY and ERA5, and is dominant in the stratosphere. Eastward (westward) propagation is more frequent than westward (eastward) propagation in the stratosphere (troposphere) for both PANSY and ERA5.

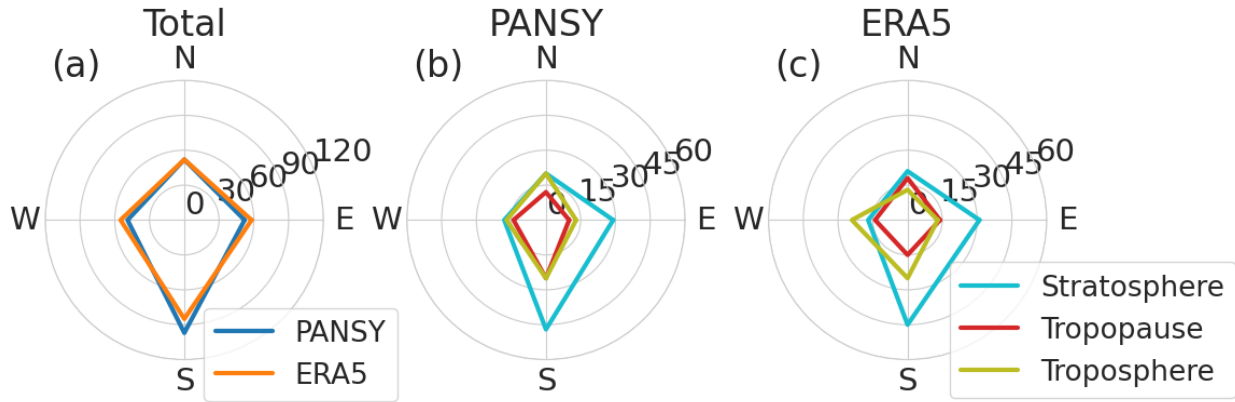


Figure 9. Radar charts of propagation directions of GWs for east-, west-, north-, and south-ward. (a) All altitude ranges for PANSY (blue) and ERA5 (orange); the troposphere (olive), tropopause (red), and stratosphere (blue) for (b) PANSY and (c) ERA5.

5 Discussion

5.1. Characteristics of large-amplitude inertia GWs above Syowa Station

Minamihara et al. (2018) applied hodograph analysis to PANSY radar data from October 2015 to September 2016 to investigate the characteristics of inertia GWs over Syowa Station. This study applied the same hodograph analysis to the PANSY radar and ERA5 data for the same period. However, whereas Minamihara et al. (2018) applied hodograph analysis to individual vertical profiles to extract all inertia GWs, this study extracted large-amplitude GW events corresponding to the top 10% of AMFs and focused on long-lasting inertia GWs captured in multi-time vertical profiles. We compared the results obtained from our hodograph analysis with those of Minamihara et al. (2018) and considered the characteristics of large-amplitude inertia GWs over Syowa Station.

Large-amplitude inertia GWs over Syowa Station are dominated by those with $C_z < 0$ as the altitude increases (see section 3.4). In addition, seasonal variation is larger at higher altitudes

(i.e., the stratosphere), where inertia GWs with $C_z < 0$ are most frequent in austral autumn and those with $C_z > 0$ are more frequent in austral winter. These characteristics are consistent with those of Minamihara et al. (2018) and suggest that topography, tropospheric jets, and polar night jet are the main sources of inertia GW excitation, which also applies to large-amplitude inertia GWs.

The intrinsic period of inertia GWs tends to be longer, the vertical wavelength is shorter, and the horizontal wavelength increases as altitude increases (see section 3.4). These features are consistent with Minamihara et al. (2018). On the other hand, the vertical wavelength is approximately 4 km in the troposphere and 3 km in the stratosphere, and the horizontal wavelength is approximately 250 km in the troposphere and 500–700 km in the stratosphere. These values are greater than those reported by Minamihara et al. (2018). This difference suggests that inertia GWs with large amplitudes tend to have longer horizontal and vertical wavelengths.

The propagation direction of inertia GWs is generally dominated by a southward component, which is particularly pronounced in the stratosphere. In addition, the propagation direction tends to be more eastward in the stratosphere and westward in the troposphere. This small directional preference in the troposphere is consistent with the findings of Minamihara et al. (2018). However, the predominance of southward propagation in the stratosphere has not been reported, and could be an inherent feature of large-amplitude inertia GWs. In view of the fact that the power spectrum of horizontal winds with $C_z < 0$ has a peak near the inertial period in the stratosphere (see Fig. 7), our results may reflect southward propagation of GWs generated by tropical convective activity, as described by Sato et al. (1999).

5.2. AMF difference between PANSY and ERA5

The AMF of ERA5 is ~ 0.2 times that of PANSY in the troposphere and decreases with altitude in the stratosphere to ~ 0.05 at 20 km altitude (see section 4.1). Horizontal winds have similar power near the inertial period; however, the spectral slope of ERA5 is steeper than that of PANSY (see section 4.2). The power spectra of the vertical winds are approximately one order of magnitude larger in PANSY, even near the inertial period, and the difference increases at higher frequencies. We compared the results of the hodograph analysis of large-amplitude inertia GWs and showed that ERA5 underestimates the vertical wind amplitude (see section 4.3). Therefore, we examined whether the difference in the power spectra between PANSY and ERA5 can quantitatively explain the difference in AMF.

Jewtoukoff et al. (2015) compared the horizontal distribution of AMF obtained from super-pressure balloon observations with operational analysis data from ECMWF and reported that AMF calculated from ECMWF data was approximately 1/3 to 1/5 of that from super-pressure balloon observations. They demonstrated that the difference in the AMF between the two can be largely explained by the difference in their resolvable horizontal wavenumber ranges. Since PANSY radar observations, unlike super-pressure balloon observations, provide time–height cross sections of AMF at Syowa Station, we attempted to explain the difference not in terms of horizontal wavenumber but in terms of the frequency range in which GWs can be resolved.

Jewtoukoff et al. (2015) assumed that the operational analysis of ECMWF data can reproduce GWs with horizontal wavenumbers smaller than a certain cutoff wavenumber, and

that for larger wavenumbers, their amplitudes are zero. However, as shown in Fig. 7, the frequency spectra of horizontal and vertical winds in ERA5 do not become zero at any cutoff frequency but show spectra with a different slope from PANSY in the entire frequency range of GWs. Figure 10 shows hypothetical regions in the horizontal and vertical wavenumber spaces, where PANSY and ERA5 can resolve, by oblique lines and shading, respectively. The dashed-dotted lines represent the isopleths of the intrinsic wave period obtained from the dispersion relation of inertia GWs (Eq. 2). PANSY can capture almost any period over a wide range of horizontal and vertical wavenumber regions, whereas ERA5 can resolve narrower horizontal and vertical wavenumber regions as the period decreases. In other words, it can be considered that the shorter the period (i.e., higher frequency), the narrower the resolvable region becomes, which is reflected in the difference in the slope of the frequency spectrum.

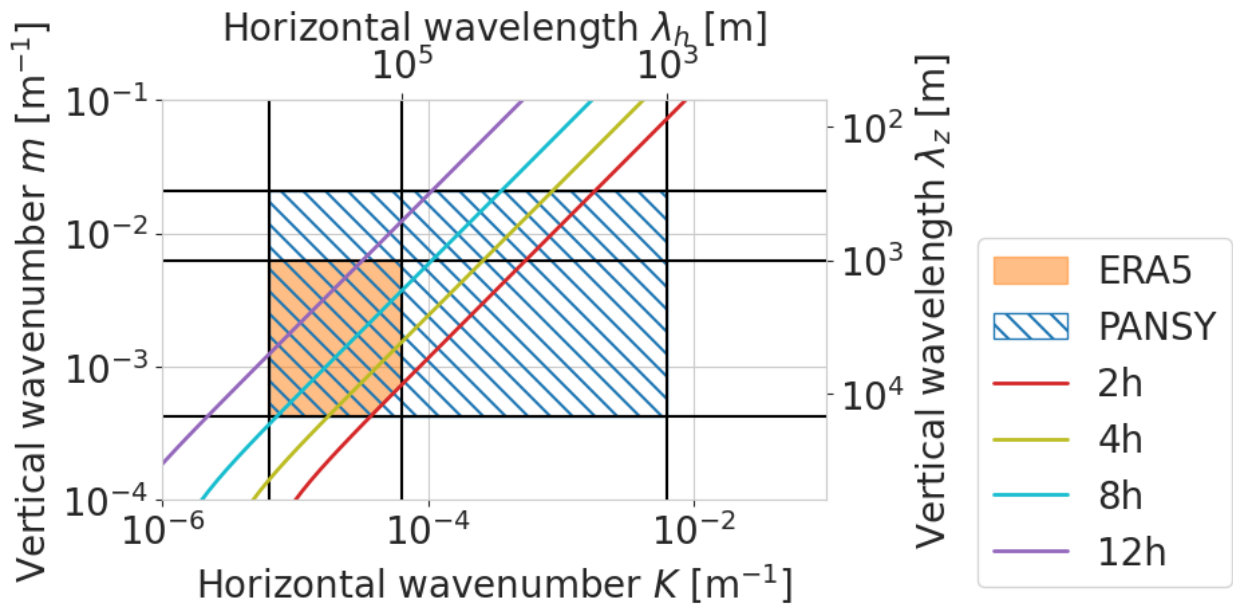


Figure 10. Hypothetical regions in horizontal and vertical wavenumber space where PANSY and ERA5 can resolve are shown by oblique lines and shading, respectively. Solid lines represent isopleths of intrinsic wave period obtained from the dispersion relationship of inertia GWs (i.e., Eq. 2).

Suppose the frequency power spectra of the horizontal and vertical winds in an energy content form follow the power law:

$$fP(f) = b(f)^a \#(10)$$

where f is the frequency normalized by the inertial frequency f_i , a is the exponent of the spectral slope, and b is the power at f_i . By integrating it over the frequency range of inertia GWs between $f = 1$ and $f = f_h = 2\pi/4h/f_i$, the AMF ratio between PANSY and ERA5 can be obtained as follows (see Liu (2019)):

$$\text{AMFratio}\left(\frac{\text{ERA5}}{\text{PANSY}}\right) = \frac{b_{u\text{ERA5}}b_{w\text{ERA5}}}{b_{u\text{PANSY}}b_{w\text{PANSY}}} \frac{\frac{1 - (f_h)^{\frac{a_{u\text{ERA5}} + a_{w\text{ERA5}}}{2}}}{a_{u\text{ERA5}} + a_{w\text{ERA5}}}}{\frac{1 - (f_h)^{\frac{a_{u\text{PANSY}} + a_{w\text{PANSY}}}{2}}}{a_{u\text{PANSY}} + a_{w\text{PANSY}}}}, \#(11)$$

where subscripts u and w represent horizontal and vertical wind components, respectively.

The vertical profile of the AMF ratio between PANSY and ERA5 obtained from the spectra using Eq. 11 is shown in Figure 11a. Parameters a and b were estimated from Figure 7. The AMF ratio is approximately 0.15 at altitudes of 5–12 km, which is slightly smaller than the ratio in Figure 6; however, the altitude variation is in good agreement. Thus, the difference in AMF between PANSY and ERA5 can be roughly explained by the magnitude and slope of their wind power spectra; in other words, the difference in AMF between PANSY and ERA5 depends on the range of GWs resolved in the model used for ERA5. Next, we confirmed which of the horizontal and vertical winds contribute to the underestimation of AMF in ERA5. The ratios of the power spectra of the zonal and vertical winds are shown in Figure 11a. The powers of the zonal and vertical winds in ERA5 are approximately 1/2 and 1/50 of that in PANSY, respectively. Since horizontal and vertical winds contribute to the momentum flux by the square root of their power, contributions of horizontal and vertical winds to the underestimation of AMF in ERA5 are estimated at factors of $1/\sqrt{2}$ and $1/7$, respectively.

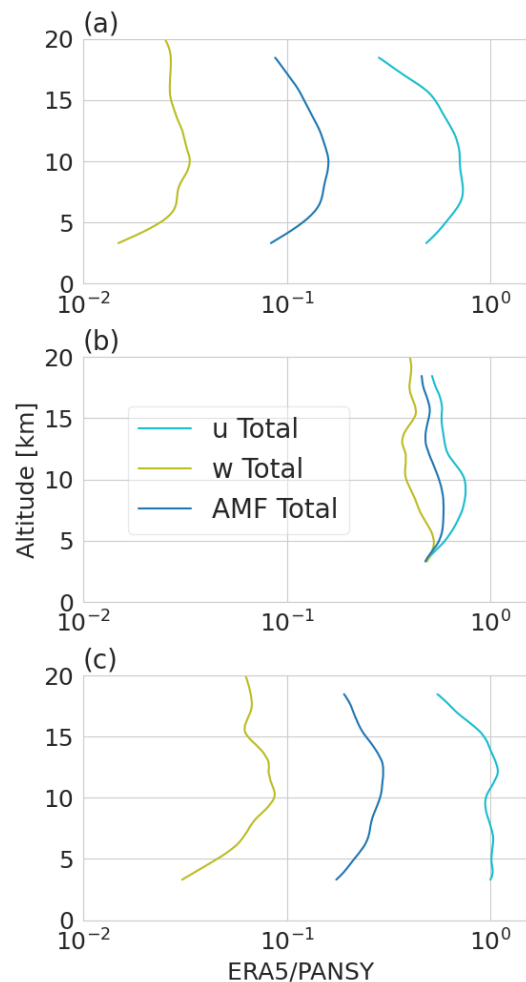


Figure 11. Vertical profiles of power spectra of u (cyan), power spectra of w (olive), and the AMF ratio (ERA5/PANSY) (blue) with no assumptions (a), when the power at f_i (i.e., parameter b) is assumed to be the same between PANSY and ERA5 (b), and when the spectral slope (i.e., parameter a) is assumed to be the same between PANSY and ERA5 (c).

The relative contributions of parameters a and b were also examined. Figure 11b shows the vertical profile of the AMF ratio when the power at f_i (i.e., parameter b) was assumed to be the same for PANSY and ERA5. ERA5 underestimates AMF by approximately 1/2 owing to the difference in parameter a (i.e., spectral slope). The contribution of parameter a for the vertical wind to the underestimation of AMF in ERA5 is slightly larger than that for the zonal wind. The contribution of parameter b , assuming that parameter a is the same for PANSY and ERA5, is shown in Figure 11c. It was found that ERA5 underestimates AMF by approximately 1/4 owing to the difference in parameter b (i.e., power at f_i). Although this is mostly due to the underestimation of parameter b for vertical winds, the contribution of parameter b for zonal winds increases with altitude above 12.5 km.

The above analysis shows that the underestimation of AMF in ERA5 can be largely explained by the underestimation of horizontal and vertical wind spectra. As shown in Figure 10, it can be inferred that underestimation of the spectra is mainly due to the limited resolution of the model used in the ERA5. However, it is not clear why the underestimation of AMF in ERA5

increases with altitude above 12.5 km. Figure 11c shows that above 12.5 km altitude, the power at f_i in ERA5 is smaller than that in PANSY, not only for the vertical wind but also for the zonal wind. Although the vertical grid spacing in the ERA5 model is approximately 300 m in the middle and upper troposphere, it increases with altitude above approximately 12 km (Hersbach et al., 2020). This suggests that the vertical wavenumber range of GWs resolved by the ERA5 model may decrease with altitude. In addition, the vertical wavelengths of the dominant inertia GWs become shorter with increasing altitude (see section 4.3). Wicker et al. (2023) also demonstrated that GW potential energy in the ECMWF IFS model, which was the same as that used for ERA5, was smaller in the model version with 91 vertical levels than in that with 198 vertical levels in the polar stratosphere during a sudden stratospheric warming event, suggesting importance of vertical resolution for the representation of GWs. Therefore, both the coarsening of the vertical resolution with altitude, and the shortening of the dominant vertical wavelength of GWs may contribute to the larger underestimation of AMF with altitude in ERA5.

6 Conclusion

The characteristics of large-amplitude inertia GWs over Syowa Station, Antarctica, were examined and compared between PANSY radar observations and ERA5 reanalysis data from October 2015 to September 2016. Focusing on large-amplitude events with a large AMF, hodograph analysis was applied to estimate the wave parameters. The percentage of large-amplitude GWs with a downward phase velocity increased with altitude. Their vertical wavelengths and intrinsic periods became shorter and longer with increasing altitude, respectively, resulting in longer horizontal wavelengths. In addition, the southward propagation of the GWs was predominant, especially in the stratosphere. Compared with the results of Minamihara et al. (2018), who applied a similar hodograph analysis to the PANSY radar data for the same period and included inertia GWs with small amplitudes, the altitude variation of the wave parameters was the same, whereas the dominant horizontal and vertical wavelengths were longer. In addition, Minamihara et al. (2018) did not report the dominance of southward propagation in the stratosphere. Thus, these features are considered to be characteristic of large-amplitude inertia GWs over Syowa Station.

Next, we compared the AMF obtained by PANSY and ERA5 to verify how well ERA5 represented momentum transport due to GWs. The results show that ERA5 underestimates AMF by approximately 1/5 at altitudes between 5 and 12.5 km; the degree of underestimation increases at altitudes above 12.5 km. AMF was estimated from the power spectra of the horizontal and vertical winds and compared with the above results. It was found that the underestimation of AMF in ERA5 can be explained by the underestimation of the power spectra of horizontal and vertical winds, especially vertical winds. The larger degree of underestimation with altitude in the stratosphere may be due to the larger vertical grid spacing of the ERA5 model with altitude, and the shorter dominant vertical wavelength of GWs with altitude.

In this study, we examined how well large-amplitude inertia GWs are quantitatively represented in ERA5. However, the relationship between the degree of GW representation in ERA5 and wave sources is unclear and should be investigated in future studies. Although GWs over Syowa Station are considered to be mostly caused by topography, tropospheric jets, and polar night jets, observations at different locations where GWs from different wave sources may predominate, or horizontal distribution observations using super-pressure balloons may be effective.

Acknowledgments

The PANSY radar was operated by Japanese Antarctic Research Expedition (JARE). This work was supported by the JST SPRING (grant number JPMJSP2104).

Data Availability Statement

The PANSY radar observation data is available at <http://pansy.eps.s.u-tokyo.ac.jp/en/data/nc.php> [Dataset]. The ERA5 on model levels are available from the Copernicus Climate Data Store at <https://cds.climate.copernicus.eu/cdsapp#!/dataset/reanalysis-era5-complete> [Dataset]. The processed data from the PANSY radar observations are available from Yoshida et al. (2023) at <https://doi.org/10.5281/zenodo.10183708> [Dataset].

References

- Alexander, M. J., Geller, M., McLandress, C., Polavarapu, S., Preusse, P., Sassi, F., et al. (2010). Recent developments in gravity-wave effects in climate models and the global distribution of gravity-wave momentum flux from observations and models. *Quarterly Journal of the Royal Meteorological Society*, 136(650), 1103–1124. <https://doi.org/10.1002/qj.637>
- Andrews, D. G., Holton, J. R., & Leovy, C. B. (1987). *Middle Atmosphere Dynamics*. Orlando: Academic Press. (Vol. 40). <https://doi.org/10.1038/294519a0>
- Becker, E., & Vadas, S. L. (2020). Explicit Global Simulation of Gravity Waves in the Thermosphere. *Journal of Geophysical Research: Space Physics*, 125(10), 1–47. <https://doi.org/10.1029/2020JA028034>
- Boccara, G., Hertzog, A., Vincent, R. A., & Vial, F. (2008). Estimation of gravity wave momentum flux and phase speeds from quasi-lagrangian stratospheric balloon flights. Part I: Theory and simulations. *Journal of the Atmospheric Sciences*, 65(10), 3042–3055. <https://doi.org/10.1175/2008JAS2709.1>
- Charron, M., & Manzini, E. (2002). Gravity waves from fronts: Parameterization and middle atmosphere response in a general circulation model. *Journal of the Atmospheric Sciences*, 59(5), 923–941. [https://doi.org/10.1175/1520-0469\(2002\)059<0923:GWFFPA>2.0.CO;2](https://doi.org/10.1175/1520-0469(2002)059<0923:GWFFPA>2.0.CO;2)
- Eckermann, S. O., & Preusse, P. (1999). Global measurements of stratospheric mountain waves from space. *Science*, 286(5444), 1534–1537. <https://doi.org/10.1126/science.286.5444.1534>
- Ern, M., Hoffmann, L., Rhode, S., & Preusse, P. (2022). The Mesoscale Gravity Wave Response to the 2022 Tonga Volcanic Eruption: AIRS and MLS Satellite Observations and Source Backtracing. *Geophysical Research Letters*, 49(10). <https://doi.org/10.1029/2022GL098626>
- Ern, M., Preusse, P., & Riese, M. (2022). Intermittency of gravity wave potential energies and absolute momentum fluxes derived from infrared limb sounding satellite observations. *Atmospheric Chemistry and Physics*, 22(22), 15093–15133. <https://doi.org/10.5194/acp-22-15093-2022>

- Fovell, R., Durran, D., & Holton, J. R. (1992). Numerical Simulations of Convectively Generated Stratospheric Gravity Waves. *Journal of the Atmospheric Sciences*, 49(16), 1427–1442. [https://doi.org/10.1175/1520-0469\(1992\)049<1427:NSOCGS>2.0.CO;2](https://doi.org/10.1175/1520-0469(1992)049<1427:NSOCGS>2.0.CO;2)
- Geldenhuys, M., Preusse, P., Krisch, I., Zülicke, C., Ungermann, J., Ern, M., et al. (2021). Orographically induced spontaneous imbalance within the jet causing a large-scale gravity wave event. *Atmospheric Chemistry and Physics*, 21(13), 10393–10412. <https://doi.org/10.5194/acp-21-10393-2021>
- Hersbach, H., Bell, B., Berrisford, P., Hirahara, S., Horányi, A., Muñoz-Sabater, J., et al. (2017). Complete ERA5 from 1940: Fifth generation of ECMWF atmospheric reanalyses of the global climate. Copernicus Climate Change Service (C3S) Data Store (CDS) [Dataset]. <https://doi.org/10.24381/cds.143582cf> (Accessed on 04-May-2022)
- Hersbach, H., Bell, B., Berrisford, P., Hirahara, S., Horányi, A., Muñoz-Sabater, J., et al. (2020). The ERA5 global reanalysis. *Quarterly Journal of the Royal Meteorological Society*, 146(730), 1999–2049. <https://doi.org/10.1002/qj.3803>
- Hertzog, A., Alexander, J. M., & Plougonven, R. (2012). On the intermittency of gravity wave momentum flux in the stratosphere. *Journal of the Atmospheric Sciences*, 69(11), 3433–3448. <https://doi.org/10.1175/JAS-D-12-09.1>
- Jewtoukoff, V., Hertzog, A., Plougonven, R., de la Cámara, A., & Lott, F. (2015). Comparison of gravity waves in the southern hemisphere derived from balloon observations and the ECMWF analyses. *Journal of the Atmospheric Sciences*, 72(9), 3449–3468. <https://doi.org/10.1175/JAS-D-14-0324.1>
- Kim, Y. H., Chun, H. Y., Park, S. H., Song, I. S., & Choi, H. J. (2016). Characteristics of gravity waves generated in the jet-front system in a baroclinic instability simulation. *Atmospheric Chemistry and Physics*, 16(8), 4799–4815. <https://doi.org/10.5194/acp-16-4799-2016>
- Kruse, C. G., Alexander, M. J., Hoffmann, L., Niekerk, A. V. A. N., Polichtchouk, I., Bacmeister, J. T., et al. (2022). Observed and Modeled Mountain Waves from the Surface to the Mesosphere near the Drake Passage. *Journal of the Atmospheric Sciences*, 79(4), 909–932. <https://doi.org/10.1175/JAS-D-21-0252.1>
- Liu, H. L. (2019). Quantifying gravity wave forcing using scale invariance. *Nature Communications*, 10(1), 1–12. <https://doi.org/10.1038/s41467-019-10527-z>
- Lott, F., & Miller, M. J. (1997). A new subgrid-scale orographic drag parametrization: Its formulation and testing. *Quarterly Journal of the Royal Meteorological Society*, 123(537), 101–127. <https://doi.org/10.1002/qj.49712353704>
- McFarlane, N. A. (1987). The Effect of Orographically Excited Gravity Wave Drag on the General Circulation of the Lower Stratosphere and Troposphere. *Journal of the Atmospheric Sciences*, 44(14), 1775–1800. [https://doi.org/10.1175/1520-0469\(1987\)044<1775:TEOOEG>2.0.CO;2](https://doi.org/10.1175/1520-0469(1987)044<1775:TEOOEG>2.0.CO;2)
- McLandress, C., Shepherd, T. G., Polavarapu, S., & Beagley, S. R. (2012). Is missing orographic gravity wave drag near 60°s the cause of the stratospheric zonal wind biases in chemistry-

- climate models? *Journal of the Atmospheric Sciences*, 69(3), 802–818.
<https://doi.org/10.1175/JAS-D-11-0159.1>
- Minamihara, Y., Sato, K., Kohma, M., & Tsutsumi, M. (2016). Characteristics of vertical wind fluctuations in the lower troposphere at syowa station in the antarctic revealed by the PANSY radar. *Scientific Online Letters on the Atmosphere*, 12, 116–120.
<https://doi.org/10.2151/sola.2016-026>
- Okui, H., Wright, C. J., Hindley, N. P., Lear, E. J., & Sato, K. (2023). A Comparison of Stratospheric Gravity Waves in a High-Resolution General Circulation Model With 3-D Satellite Observations. *Journal of Geophysical Research: Atmospheres*, 128(13).
<https://doi.org/10.1029/2023JD038795>
- Oyama, S., & Watkins, B. J. (2012). Generation of atmospheric gravity waves in the polar thermosphere in response to auroral activity. *Space Science Reviews*, 168(1–4), 463–473.
<https://doi.org/10.1007/s11214-011-9847-z>
- Piani, C., Durran, D., Alexander, M. J., & Holton, J. R. (2000). A numerical of three-dimensional gravity waves triggered by deep tropical convection and their role in the dynamics of the QBO. *Journal of the Atmospheric Sciences*, 57(22), 3689–3702.
[https://doi.org/10.1175/1520-0469\(2000\)057<3689:ANSOTD>2.0.CO;2](https://doi.org/10.1175/1520-0469(2000)057<3689:ANSOTD>2.0.CO;2)
- Plougonven, R., & Zhang, F. (2014). Internal gravity waves from atmospheric jets and fronts. *Reviews of Geophysics*, 52(1), 33–76. <https://doi.org/10.1002/2012RG000419>
- Preusse, P., Eckermann, S. D., & Ern, M. (2008). Transparency of the atmosphere to short horizontal wavelength gravity waves. *Journal of Geophysical Research Atmospheres*, 113(24), 1–16. <https://doi.org/10.1029/2007JD009682>
- Sato, K., Kumakura, T., & Takahashi, M. (1999). Gravity waves appearing in a high-resolution GCM simulation. *Journal of the Atmospheric Sciences*, 56(8), 1005–1018.
[https://doi.org/10.1175/1520-0469\(1999\)056%3C1005:GWAIAH%3E2.0.CO;2](https://doi.org/10.1175/1520-0469(1999)056%3C1005:GWAIAH%3E2.0.CO;2)
- Sato, K., Watanabe, S., Kawatani, Y., Tomikawa, Y., Miyazaki, K., & Takahashi, M. (2009). On the origins of mesospheric gravity waves. *Geophysical Research Letters*, 36(19), 1–5.
<https://doi.org/10.1029/2009GL039908>
- Sato, K., Tsutsumi, M., Sato, T., Nakamura, T., Saito, A., Tomikawa, Y., et al. (2014). Program of the Antarctic Syowa MST/IS radar (PANSY). *Journal of Atmospheric and Solar-Terrestrial Physics*, 118, 2–15. <https://doi.org/10.1016/j.jastp.2013.08.022>
- Stephan, C. C., Strube, C., Klocke, D., Ern, M., Hoffmann, L., Preusse, P., & Schmidt, H. (2019). Gravity Waves in Global High-Resolution Simulations With Explicit and Parameterized Convection. *Journal of Geophysical Research: Atmospheres*, 124(8), 4446–4459.
<https://doi.org/10.1029/2018JD030073>
- Tomikawa, Y., Nishimura, Y., & Yamanouchi, T. (2009). Characteristics of tropopause and tropopause inversion layer in the polar region. *SOLA*, 5, 141–144.
- Vadas, S. L., Becker, E., Bossert, K., Baumgarten, G., Hoffmann, L., & Harvey, V. L. (2023). Secondary Gravity Waves From the Stratospheric Polar Vortex Over ALOMAR Observatory on 12–14 January 2016: Observations and Modeling. *Journal of*

Geophysical Research: Atmospheres, 128(2), 1–37.
<https://doi.org/10.1029/2022JD036985>

Wei, J., Zhang, F., & Richter, J. H. (2016). An analysis of gravity wave spectral characteristics in moist baroclinic jet-front systems. *Journal of the Atmospheric Sciences*, 73(8), 3133–3155. <https://doi.org/10.1175/JAS-D-15-0316.1>

Wicker, W., Polichtchouk, I., & Domeisen, D. I. V. (2023). Increased vertical resolution in the stratosphere reveals role of gravity waves after sudden stratospheric warmings. *Weather Clim. Dynam.*, 4, 81–93. <https://doi.org/10.5194/wcd-4-81-2023>

Yoshida, L., Tomikawa, Y., Ejiri M. K., Tsutsumi M., Kohma M., & Sato K. (2023). The processed data from the PANSY radar observations and the ERA5 analysis [Dataset]. <https://doi.org/10.5281/zenodo.10183708>

Yoshiki, M., Kizu, N., & Sato, K. (2004). Energy enhancements of gravity waves in the Antarctic lower stratosphere associated with variations in the polar vortex and tropospheric disturbances. *Journal of Geophysical Research D: Atmospheres*, 109(23), 1–12. <https://doi.org/10.1029/2004JD004870>

Zhang, F. (2004). Generation of mesoscale gravity waves in upper-tropospheric jet-front systems. *Journal of the Atmospheric Sciences*, 61(4), 440–457. [https://doi.org/10.1175/1520-0469\(2004\)061<0440:GOMGWI>2.0.CO;2](https://doi.org/10.1175/1520-0469(2004)061<0440:GOMGWI>2.0.CO;2)